# Time-dependent simulation of cavitating flow with k-l turbulence models

Jean Decaix, Eric Goncalvès da Silva

# Time-Dependent Simulation of Cavitating Flow with $k - \ell$ Turbulence Models

Jean Decaix and Eric Goncalvès[*]

*LEGI, Grenoble INP, 1025 rue de la Piscine, 38400 St Martin d'Heres, France*

## SUMMARY

A compressible, multiphase, one-fluid RANS solver has been developed to study turbulent cavitating flows. The interplay between turbulence and cavitation regarding the unsteadiness and structure of the flow is complex and not well understood. This constitutes a critical point to accurately simulate the dynamic behaviour of sheet cavities. In the present study, different formulations based on a $k - \ell$ transport-equation model are investigated and a scale-adaptive formulation is proposed. Numerical results are given for a Venturi geometry and comparisons are made with experimental data. The scale-adaptive model shows several improvements compared to standard turbulence models. Copyright © 2010 John Wiley & Sons, Ltd.

## 1. INTRODUCTION

The simulation of cavitating flows is a challenging problem both in the modelling of the physics involved and in developing robust numerical methodologies. Such flows are characterized by

---

[*]Correspondence to: Eric Goncalvès, LEGI, Grenoble INP, 1025 rue de la Piscine, 38400 St Martin d'Heres, France.
E-mail: Eric.Goncalves@legi.grenoble-inp.fr

important variations of the local Mach number, compressibility effects on turbulence, and thermodynamic phase transition. For the simulation of these flows, the numerical method must accurately handle any Mach number. Moreover, the modelling of turbulence plays a major role in the correct simulation of unsteady behaviours. Sheet cavitation that appear on solid bodies are characterized by a closure region which always fluctuates, with the presence of a re-entrant jet. This jet is mainly composed of liquid which flows upstream along the solid surface. Reynolds-Averaged Navier-Stokes (RANS) models are frequently used to simulate such unsteady cavitating flows. One fundamental problem with this approach is that turbulence models are tuned by steady-state non-cavitating mean flow data. Moreover, the standard eddy-viscosity models based on the Boussinesq relation are known to over-produce eddy-viscosity, which reduces the development of the re-entrant jet and two-phase structure shedding [1]. Limitation of the turbulent viscosity is therefore a determining point to correctly simulate cavitation sheets. Different strategies have been investigated to limit or to correct standard turbulence models. An arbitrary modification was proposed by Reboud to reduce the turbulent viscosity [1], and has been used successfully by different authors [2, 3]. Other corrections are based on the modelling of compressibility effects of the vapour/liquid mixture in the turbulence model. Correction terms proposed by Wilcox [4] in the case of compressible flows were tested for unsteady periodic cavitating flows [2]. A sensitivity analysis of constants $C_{\varepsilon 1}$ and $C_{\varepsilon 2}$, which directly influence the production and dissipation of turbulence kinetic energy, was conducted for a $k - \varepsilon$ model and a cavitating hydrofoil case [5]. Finally, a filter-based method was investigated [6] by which the sub-filter stresses are constructed directly using the filter size and the $k - \varepsilon$ turbulence closure.

In previous works, an in-house finite-volume code solving the Reynolds-Averaged Navier-Stokes (RANS) compressible equations was developed with homogeneous approach. The cavitation phenomenon is modelled by a barotropic liquid-vapour mixture equation of state (EOS). Preliminary computations were performed to assess the numerical aspects and thermodynamic constrains on the EOS [7, 8]. The influence of various transport equation turbulence models with

different eddy-viscosity limiters were investigated [9].

This paper presents the latest work in which particular emphasis is placed on the study of a new scale-adaptive turbulence model and the investigation of eddy-viscosity corrections for flows involving a sheet cavity. The purpose of the study is to provide an alternative to the Reboud empirical correction with a better theoretical fundament. All tests are performed with the Smith $k - \ell$ model [10] to simulate a sheet cavity for a Venturi geometry. Three different eddy-viscosity limiters are considered: the Reboud correction [1], the shear stress transport (SST) correction developed by Menter [11, 12] and a variant of the latter based on realizability constraints [13]. Following Menter's developments concerning the Scale-Adaptive Simulation (SAS) [14, 15], a new $k - \ell$ SAS model is proposed.

The Scale-Adaptive Simulation first appeared in the formulation of the KE1E one-equation model for the eddy-viscosity derived from the standard $k - \varepsilon$ model [16]. The transformation from the $k - \varepsilon$ model to the KE1E model introduces the von Karman length-scale $L_{vK}$. The KE1E model provides a dynamical behaviour similar to a Detached Eddy Simulation (DES) model but without an explicit grid dependence, allowing the development of a turbulent spectrum in the detached regions. Later, Menter and Egorov [17] showed that the exact transport equation for the turbulent length scale $l$ as derived by Rotta actually introduces the second derivative of the velocity field. They proposed a model for this term which introduces the von Karman length-scale. Then, they inserted this term (referred to as SAS) in the existing two-equation models. Starting from the two-equation model for the variable $k$ and $\sqrt{k}l$ including the SAS term, they derived a SST-SAS model by a variable change. They calibrated the SST-SAS model for the decay of a homogeneous isotropic turbulence[14]. Various test cases [15, 18] were also conducted such as flow around a cylinder, which showed the ability of the SST-SAS model to resolve turbulent structures down to the limit grid. Davidson [19] performed other test cases with the SST-SAS model such as channel flow, asymmetric diffuser flow and flow over a three-dimensional hill. These test cases confirmed that the SAS term reduces the turbulent eddy-viscosity and predicts resolved fluctuations much

4

larger than standard models.

In this paper, we will first review the theoretical formulation, including physical models and elements of the numerical methods, then we will present and discuss results for a Venturi geometry.

## 2. GOVERNING EQUATIONS AND MODELS

The numerical simulations are carried out using an in-house CFD code solving the one-fluid compressible RANS system.

The homogeneous model assumes that the two phases are strongly coupled and moving at the same velocity. The phases are assumed to share the same temperature $T$ and the same pressure $P$. The evolution of the two-phase flow can be described by Euler equations that employ the representative flow properties as unknowns just as in a single-phase problem. The mixture density $\rho$ is defined by:

$$\rho = \alpha\rho_V + (1-\alpha)\rho_L \tag{1}$$

where $\rho_L$ and $\rho_V$ are respectively the liquid and vapour densities. The void ratio $\alpha$ characterizes the volume of vapour in each cell: $\alpha = 1$ means that the cell is completely filled by vapour and inversely, a complete liquid cell is represented by $\alpha = 0$. Liquid and vapour phases are characterized by their thermodynamic properties. On each cell, the unknowns are calculated by averaging them over the volume occupied.

### 2.1. Reynolds-Averaged Navier-Stokes equations

For turbulent computations, the Reynolds-averaged compressible equations are used, coupled with two-equation turbulence models. For low Mach number applications, an inviscid preconditioning method is necessary [20, 21], based on the modification of the derivative term by a pre-multiplication with a suitable preconditioning matrix $P_c$. These equations can be expressed as:

$$P_c^{-1}\frac{\partial w}{\partial t} + \text{div}\,(F_c - F_v) = S \tag{2}$$

$$
w = \begin{pmatrix} \rho \\ \rho V \\ \rho E \\ \rho k \\ \rho \Psi \end{pmatrix} \quad ; \quad F_c = \begin{pmatrix} \rho V \\ \rho V \otimes V + p\bar{\bar{I}} \\ (\rho E + p)V \\ \rho k V \\ \rho \Psi V \end{pmatrix} \quad ; \quad F_v = \begin{pmatrix} 0 \\ \bar{\bar{\tau^v}} + \bar{\bar{\tau^t}} \\ (\bar{\bar{\tau^v}} + \bar{\bar{\tau^t}}).V - Q^v - Q^t \\ (\mu + \mu_t/\sigma_k)\,\mathrm{grad}\,k \\ (\mu + \mu_t/\sigma_\Psi)\,\mathrm{grad}\,\Psi \end{pmatrix}
$$

where $w$ denotes the conservative variables, $F_c$ and $F_v$ the convective and viscous flux densities and $S$ the source terms, which concern only the transport equations. $k$ is the turbulent kinetic energy and $\Psi$ is a turbulent variable.

The exact expression of the eddy-viscosity $\mu_t$ and the source terms depends on the turbulence model as well as constants $\sigma_k$ and $\sigma_\Psi$.

The total stress tensor $\bar{\bar{\tau}}$ is evaluated using the Stokes hypothesis, Newton's law and the Boussinesq assumption. The total heat flux vector $Q$ is obtained from the Fourier law with thermal conductivities $\lambda$ and the constant Prandtl number hypothesis. The turbulent Prandtl number $P_{rt}$ is set to 1.

$$
\begin{aligned}
\bar{\bar{\tau}} &= \bar{\bar{\tau^v}} + \bar{\bar{\tau^t}} = (\mu + \mu_t)\left[(\,\mathrm{grad}\,V + (\,\mathrm{grad}\,V)^t) - \frac{2}{3}(\,\mathrm{div}\,V)\bar{\bar{I}}\right] + \frac{2}{3}k\bar{\bar{I}} \\
Q &= Q^v + Q^t = -(\lambda + \lambda_t)\,\mathrm{grad}\,T \qquad \text{with} \quad \lambda_t = \frac{\mu_t C_p}{P_{rt}}
\end{aligned} \tag{3}
$$

In pure liquid, the viscosity is determined by an exponential law and, in pure vapour, the viscosity follows the Sutherland law. The mixture viscosity $\mu$ is calculated as the arithmetic mean of the liquid and vapour viscosities:

$$
\mu_L(T) = \mu_{0_L}\exp\left(B/T\right) \tag{4}
$$

$$
\mu_V(T) = \mu_{0_V}\sqrt{\frac{T}{293}}\frac{1 + T_S/293}{1 + T_S/T} \tag{5}
$$

$$
\mu(T, \alpha) = \alpha\mu_V(T) + (1 - \alpha)\mu_L(T) \tag{6}
$$

where $\mu_{0_L}$, $\mu_{0_V}$, $B$ and $T_S$ are constants.

6

The mixture thermal conductivity $\lambda$ is also defined as the arithmetic mean of the liquid and vapour values:

$$\lambda(\alpha) = \alpha \frac{\mu_V C_{pv}}{P_{r_V}} + (1-\alpha) \frac{\mu_L C_{p_L}}{P_{r_L}} \qquad (7)$$

*2.2. The cavitation model*

To close the system, an equation of state (EOS) is necessary to link the pressure to the thermodynamic variables. Pure phases follow the stiffened gas EOS. The barotropic law proposed by Delannoy [22] is considered for the mixture.

This law is characterized by its maximum slope $1/c_{baro}^2$. The quantity $c_{baro}$ is an adjustable parameter of the model, which can be interpreted as the minimum speed of sound in the mixture. When the pressure is between $P_{vap} + \Delta P$ and $P_{vap} - \Delta P$, the following relationship applies:

$$P(\alpha) = P_{vap} + \left( \frac{\rho_L^{sat} - \rho_V^{sat}}{2} \right) c_{baro}^2 \operatorname{Arcsin}(1 - 2\alpha) \qquad (8)$$

where $\Delta P$ represents the pressure range of the law and, for a void ratio value of 0.5, the pressure is equal to the saturation pressure $P_{vap}$. This law introduces a small non-equilibrium effect on the pressure. The cavitation phenomenon is assumed to be isothermal, thermal effects are neglected.

The void ratio is computed with the internal energy of each phase at saturation:

$$\alpha = \frac{\rho e - \rho_L^{sat} e_L^{sat}}{\rho_V^{sat} e_V^{sat} - \rho_L^{sat} e_L^{sat}} \qquad (9)$$

The hyperbolicity and convexity of the EOS have been demonstrated in [7]. The influence of $c_{baro}$ has been studied in previous works. In the present paper, the value of $c_{baro}$ is set to 0.472 m/s, corresponding to a pressure range of $\Delta P = 175$ Pa.

*2.3. Turbulence Modelling*

The present study is based on the Smith $k - \ell$ (KL) turbulence model [10, 23] with different corrections and improvements.

Turbulence models always lead to the generation of stable cavities, because very strong turbulent eddy-viscosity $\mu_t$ inside the cavity prevents the formation of the re-entrant jet which plays the

major role in driving the instability of partial sheet cavity. The link to compressibility effects on turbulence is not clear. DNS of the supersonic boundary layer demonstrated a reduction in $k$ production as a consequence of compressibility [24, 25, 26]. In cavitating flows, the supersonic regime is reached in the mixture area because of the drastic diminution of the speed of sound. The detailed mechanisms of the interaction between turbulent flows and cavitation have not yet been clearly revealed, especially for phenomena occurring at small scales.

To limit the turbulent viscosity, one can use an eddy-viscosity limiter in the mixture area. In the present study, we propose to test and compare different eddy-viscosity limiters: the Reboud correction [1] specially developped for the two-phase flow; the Shear Stress Transport (SST) correction proposed by Menter [11, 12] to reduce the eddy-viscosity in case of positive pressure gradient and a variant of the latter based on realizability constraints [13].

Moreover, we developed a $k - \ell$ model including the scale-adaptive term [15]. This term allows the turbulence model to recognised the resolved scales in the flow and to adjust the eddy-viscosity as a consequence.

For the modelling of flow close to the wall, a two-layer wall law approach is used:

$$
\begin{aligned}
u^+ &= y^+ & &\text{if} \quad y^+ < 11.13 \\
\\
u^+ &= \frac{1}{\kappa} \ln y^+ + 5.25 & &\text{if} \quad y^+ > 11.13 \\
u^+ &= \frac{u}{U_\tau} & &; \qquad y^+ = \frac{yU_\tau}{\nu_w} \quad ; \quad U_\tau^2 = \frac{\tau_w}{\rho_w}
\end{aligned}
\tag{10}
$$

where $\kappa = 0.41$ is the von Karman constant and the subscript 'w' is used for a wall value.

We assume that wall functions are similar in a two-phase flow and in a single-phase flow. For unsteady flows, the existence of a wall law is assumed to be valid at each instant. With regard to the turbulent quantities, the production of $k$ is computed according to the formulation proposed by Viegas and Rubesin [27]. The value of $\ell$ in the first cell is obtained using a classical mixing length:

$l = \kappa y$.

*2.3.1. The Smith $k - \ell$ model* First, Smith developed a $k - k\ell$ model [23] with a unique wall function. The transport equation for $kl$ derived originally by Rotta is based on the definition of the integral length scale $\ell$, using two-point correlations of the velocity fluctuations. This approach provides a better theoretical basis compared to the heuristic arguments used for determining the $\varepsilon$ transport equation. However, the $k - k\ell$ model does not simulate the turbulent kinetic energy profiles in the viscous sublayer. To rectify this inconvenience, Smith transformed the $k - k\ell$ model to a $k - \ell$ near wall model [10]. The $\ell$ equation is derived from the $k\ell$ transport equation by a simple variable change. The Smith $k - \ell$ turbulence model reads:

$$
\begin{aligned}
\frac{\partial \rho k}{\partial t} + \operatorname{div}\left[\rho k \vec{V} - \left(\mu + \frac{\mu_t}{\sigma_k}\right)\vec{\operatorname{grad}}\,k\right] &= P_k - \frac{\rho(2k)^{3/2}}{B_1 l} - 2\mu\,\vec{\operatorname{grad}}\,\sqrt{k}.\,\vec{\operatorname{grad}}\,\sqrt{k} \\
\frac{\partial \rho \ell}{\partial t} + \operatorname{div}\left[\rho \ell \vec{V} - \left(\mu + \frac{\mu_t}{\sigma_l}\right)\vec{\operatorname{grad}}\,\ell\right] &= (2 - E_2)\frac{\rho\sqrt{2k}}{B_1}\left[1 - \left(\frac{\ell}{\kappa d}\right)^2\right] \\
&\quad - \frac{\mu_t}{\sigma_l}\frac{1}{\ell}(\vec{\operatorname{grad}}\,\ell.\,\vec{\operatorname{grad}}\,\ell)\left(\frac{\ell}{\kappa d}\right)^2 + \rho\ell\operatorname{div}\vec{V} \\
&\quad + 2\frac{\mu_t}{\sigma_l}\frac{1}{k}(\vec{\operatorname{grad}}\,\ell.\,\vec{\operatorname{grad}}\,k)
\end{aligned}
\tag{11}
$$

With:

$$
\mu_t = \mu\chi f_\mu \qquad ; \qquad \chi = \frac{\rho\sqrt{2k}\ell}{\mu B_1^{1/3}}
$$

$$
f_\mu = \left(\frac{c_1{}^4 f_1 + c_2{}^2\chi^2 + \chi^4}{c_1{}^4 + c_2{}^2\chi^2 + \chi^4}\right)^{1/4} \qquad ; \qquad f_1 = \exp\left[-50\left(\frac{\ell}{\kappa d}\right)^2\right]
$$

$$
c_1 = 25.2 \qquad ; \qquad c_2 = 2
\tag{12}
$$

Constants are:

$$
\kappa = 0.41 \quad ; \quad B_1 = 18 \quad ; \quad E_2 = 1.2 \quad ; \quad \sigma_k = \sigma_l = 1.43
$$

*2.3.2. The Reboud correction* Reboud [1] proposed an arbitrary limiter by introducing a function $f(\rho)$ in the computation of the turbulent viscosity for the $k - \varepsilon$ model:

$$
\mu_t = f(\rho)C_\mu\frac{k^2}{\varepsilon} \quad \text{with } f(\rho) = \rho_V + (1 - \alpha)^n(\rho_L - \rho_V)
\tag{13}
$$

where $n$ is a parameter set to 10.

This correction is extended to the $k - \ell$ turbulence model with the same function $f(\rho)$.

*2.3.3. The Menter SST correction* The Menter correction [11, 12] is based on the empirical Bradshaw's assumption which binds the shear stress to the turbulent kinetic energy for a two-dimensional boundary layer. The stress ratio predicted by two-equation models scales with the ratio of production $P_k$ to dissipation $\varepsilon$ as:

$$\frac{-\overline{u'v'}}{k} \; = \; \sqrt{\frac{P_k}{\varepsilon}}\sqrt{C_\mu} \qquad \text{with } C_\mu = 0.09 \tag{14}$$

Experiments showed that the quantity $-\overline{u'v'}/k \leq 0.3$. Menter devised his SST limiter from this inequality. The empirically based constraint is expressed in the case of the $k - \ell$ turbulence model as:

$$\nu_t \; = \; \min\left[\frac{\mu\chi f_\mu}{\rho}, \frac{ck}{\sqrt{2}\mid\Omega\mid F_2(y)}\right] \qquad \text{with } c = 0.3 \tag{15}$$

where $F_2$ is a blending function that tends to zero outside the boundary layer, $\Omega$ is the vorticity and $f_\mu$ is a damping function of the model.

The evolution of the ratio $-\overline{u'v'}/k$ was recently measured by [28] in the case of a cavitating mixing layer. Authors showed that this ratio decreased significantly and continuously when cavitation developed. They observed a factor 2 between the non-cavitating regime and the most severe cavitating case. As the ratio $-\overline{u'v'}/k$ is unknown for cavitating flows involving sheet cavities, we tested two lower values for the constant $c$ in the two-phase area: 0.2 and 0.1. The correction is defined as followed:

$$\begin{aligned} c = 0.3 & \quad \text{if} \quad \alpha = 0 \\ c = 0.1 \text{ or } 0.2 & \quad \text{if} \quad \alpha > 0 \end{aligned} \tag{16}$$

*2.3.4. Realizability constrains* By replacing the vorticity $\Omega$ with the stress tensor $S$ in the SST formula, a correction is derived based on the realizability principle [13].

$$\nu_t \; = \; \min\left[\frac{\mu\chi f_\mu}{\rho}, \frac{ck}{\sqrt{2}\mid S\mid F_2(y)}\right] \qquad \text{with } c = 0.3 \tag{17}$$

with:

$$S = \sqrt{2S_{ij}S_{ij}} \; ; \; S_{ij} = \frac{1}{2}\left(\frac{\partial u_i}{\partial x_j} + \frac{\partial u_j}{\partial x_i}\right) \tag{18}$$

10

In the same way as for the SST correction, we tested different values of the constant $c$ between 0.1 and 0.3 in the two-phase flow region.

*2.3.5. Scale-Adaptive Simulation model* To include the Scale-Adaptive Simulation (SAS) term into the $k - \ell$ turbulence model, we started from the $k - \phi$ SAS formulation provided by Menter and Egorov [14, 15] with $\phi = \sqrt{k}\ell$. This model reads (in high Reynolds number formulation):

$$
\begin{aligned}
\frac{\partial \rho k}{\partial t} + \frac{\partial \rho U_j k}{\partial x_j} &= P_k - c_\mu^{3/4} \rho \frac{k^{3/2}}{l} + \frac{\partial}{\partial x_j}\left(\frac{\mu_t}{\sigma_k}\frac{\partial k}{\partial x_j}\right) \\
\frac{\partial \rho \phi}{\partial t} + \frac{\partial \rho U_j \phi}{\partial x_j} &= \frac{\phi}{k} P_k \left(\xi_1 - \boldsymbol{\xi_2} \left(\frac{\mathbf{l}}{\mathbf{L_{v\kappa}}}\right)^{\mathbf{2}}\right) - \xi_3 \rho k + \frac{\partial}{\partial x_j}\left(\frac{\mu_t}{\sigma_\phi}\frac{\partial \phi}{\partial x_j}\right)
\end{aligned}
\tag{19}
$$

with the SAS term in bold in the transport equation for $\phi$ and:

$$
\frac{\mu_t}{\rho} = \nu_t = c_\mu^{1/4}\phi
$$

$$
P_k = \mu_t S^2 \quad ; \quad S = \sqrt{2 S_{ij} S_{ij}} \quad ; \quad S_{ij} = \frac{1}{2}\left(\frac{\partial U_i}{\partial x_j} + \frac{\partial U_j}{\partial x_i}\right)
$$

$$
L_{v\kappa} = \kappa \left|\frac{U'}{U''}\right| \quad ; \quad \left|U'\right| = S \quad ; \quad \left|U''\right| = \sqrt{\frac{\partial^2 U_i}{\partial x_k^2}\frac{\partial^2 U_i}{\partial x_j^2}}
$$

The constants calibrated by Menter are:

$$
\xi_1 = 0.8 \quad ; \quad \xi_2 = 1.47 \quad ; \quad \xi_3 = 0.0288 \quad ; \quad \sigma_\phi = \sigma_k = \frac{2}{3} \quad ; \quad C_\mu = 0.09
$$

By a variable change, we obtained a transport equation for $\ell$ including the SAS term (in bold).

$$
\begin{aligned}
\frac{\partial \rho \ell}{\partial t} + div\left[\rho \ell \vec{V} - \left(\mu + \frac{\mu_t}{\sigma_\phi}\right)\vec{\mathrm{grad}}\ \ell\right] &= \frac{\ell}{k} P_k \left(\xi_1 - \frac{1}{2} - \boldsymbol{\xi_2}\left(\frac{\ell}{\mathbf{L_{v\kappa}}}\right)^{\mathbf{2}}\right) \\
&+ \frac{\rho\sqrt{2k}}{B_1}\left(1 - \frac{B_1 \xi_3}{\sqrt{2}}\right) \\
&- \frac{1}{\ell}\left(\frac{\mu_t}{\sigma_\phi}\right)\vec{\mathrm{grad}}\ \ell.\vec{\mathrm{grad}}\ \ell \\
&+ \frac{1}{k}\left(\frac{\mu_t}{\sigma_\phi}\right)\vec{\mathrm{grad}}\ \ell.\vec{\mathrm{grad}}\ k \\
&+ \frac{l}{2k}\frac{\partial}{\partial x_j}\left(\mu_t \frac{\partial k}{\partial x_j}\right)\left(\frac{1}{\sigma_\phi} - \frac{1}{\sigma_k}\right)
\end{aligned}
\tag{20}
$$

We compared this transport equation with the formulation of Smith (Equation 11). Excepted the new SAS term, several terms are different because of the introduction of low Reynolds number

terms and by the choice in the Smith model to cancel the production term $\frac{\ell}{k} P_k \left( \xi_1 - \frac{1}{2} \right)$. The last term in equation (20) is zero due to the equality between $\sigma_k$ and $\sigma_\phi$.

We decided to retain the choice of Smith and to activate the SAS term only in the two-phase flow region where no information about the constant values are available in the literature.

The $k - \ell$ SAS formulation is then given by the transport equation for the turbulent kinetic energy of the Smith model (Equation 11) and a new transport equation for the turbulent length scale $\ell$:

$$
\begin{aligned}
\frac{\partial \rho \ell}{\partial t} + div \left[ \rho \ell \vec{V} - \left( \mu + \frac{\mu_t}{\sigma_l} \right) \vec{\text{grad}} \; \ell \right] \;\; = \;\; & -\mathbf{\frac{1}{k} P_k \xi_2 \left( \frac{\ell}{L_{v\kappa}} \right)^2} \\
& + (2 - E_2) \frac{\rho \sqrt{2k}}{B_1} \left[ 1 - \left( \frac{\ell}{\kappa d} \right)^2 \right] \\
& - \frac{1}{\ell} \left( \frac{\mu_t}{\sigma_\ell} \right) ( \vec{\text{grad}} \; \ell . \vec{\text{grad}} \; \ell) \left( \frac{\ell}{\kappa d} \right)^2 + \rho \ell \; div \vec{V} \\
& + 2 \frac{1}{k} \left( \frac{\mu_t}{\sigma_k} \right) ( \vec{\text{grad}} \; \ell . \vec{\text{grad}} \; k)
\end{aligned}
\tag{21}
$$

The constant $\xi_2$ is set to 1.47 as specified by Menter.

The bold term in equation 21 is the SAS term and it acts as a destruction term for $\ell$. The von Karman length scale $L_{v\kappa}$ is the key to understanding the role played by the SAS term. $L_{v\kappa}$ adjusts to the already resolved scales in a simulation and provides a length scale proportional to the size of the resolved eddies whereas a standard turbulence model always provides a length scale proportional to the shear layer. Thus the SAS term leads to a model less diffusive than the standard two-equation model and provides a reduction of the turbulent viscosity. For all calculations, the SAS term is activated only in the two-phase flow region by using a test on the void ratio $\alpha$:

$$
\begin{aligned}
\text{SAS term} \;\; &= \;\; 0 \quad\quad\quad\;\; \text{if} \;\; \alpha < 0 \\
\text{SAS term} \;\; &= \;\; -\frac{l}{k} P_k \xi_2 \left( \frac{\ell}{L_{v\kappa}} \right)^2 \;\; \text{if} \;\; \alpha > 0
\end{aligned}
\tag{22}
$$

## 3. NUMERICAL METHODS

The numerical simulations are carried out using an implicit CFD code solving the RANS/turbulent systems for multi-domain structured meshes. This solver is based on a cell-centered finite-volume discretization.

### 3.1. Spatial discretization

For the mean flow, the convective flux density vector on a cell face is computed with the Jameson scheme [29] in which the dispersive error is cancelled. The artificial viscosity includes a second-order dissipation term $D_2$ and a fourth-order dissipation term $D_4$, which involve two tunable parameters $k^{(2)}$ and $k^{(4)}$.

The viscous terms are discretized by a second-order space-centered scheme. For the turbulence transport equations, the upwind Roe scheme [30] is used to obtain a more robust method. The second-order accuracy is obtained by introducing a flux-limited dissipation [31].

### 3.2. Temporal discretization

Time integration is achieved using a low-cost implicit method [32]. The implicit method consists in solving, at each time step, a system of equations arising from the linearization of a fully implicit scheme. The main advantage of this method is that the storage of the Jacobian matrix is completely eliminated, which leads to a low-storage algorithm. More details are given in [7].

For the turbulence transport equations, the diffusive flux Jacobian matrix is replaced by its spectral radius. The source term needs special treatment [33]. Only the negative part of the source term Jacobian matrix is considered and replaced by its spectral radius. The system obtained is solved with a line-alternated Jacobi relaxation algorithm.

*3.3. Inlet and outlet boundary conditions*

The numerical treatment of boundary conditions is based on the use of the preconditioned characteristic relationships [7]. We assume that inlet and outlet areas are in a pure liquid region; no cavitation appears in these boundaries.

## 4. COMPUTATIONAL RESULTS FOR A VENTURI GEOMETRY

*4.1. Experimental conditions*

The Venturi was tested in the cavitation tunnel of the CREMHyG (Centre d'Essais de Machines Hydrauliques de Grenoble). It is characterized by a divergence angle of 4°, illustrated in Fig. 1. The edge forming the throat of the Venturi is used to fix the separation point of the cavitation cavity. This geometry is equipped with five probing holes to allow various measurements such as the local void ratio, instantaneous local speed and wall pressure (Fig. 1). However, we do not have access to measurements of turbulent quantities in the two phase-flow region. This lack of information makes turbulence models validation difficult.

The selected operating point is characterized by the following physical parameters [34]:

$U_{inlet}$ = 10.8 m/s, the inlet velocity

$\sigma_{inlet} = \dfrac{P_{inlet} - P_{vap}}{0.5\rho U_{inlet}^2} \simeq 0.55$, the cavitation parameter in the inlet section

$T_{ref} \simeq 293K$, the reference temperature

$L_{ref}$=252 mm, the reference length

$Re_{L_{ref}} = \dfrac{U_{inlet}L_{ref}}{\nu} = 2.7\,10^6$, the Reynolds number

With these parameters, a cavity length $L$ ranging from 70 mm to 85 mm is obtained. The experimental views for this geometry show a relatively stable cavity behaviour. It is characterized by an almost constant length, although the closure region always fluctuates, with the presence of a re-entrant jet and little vapour cloud shedding. For this geometry, no periodic cycles with large shedding were observed.

14

## 4.2. Mesh

The grid is a H-type topology. It contains 251 nodes in the flow direction and 62 nodes in the orthogonal direction. A special contraction of the mesh is applied in the main flow direction just after the throat to better simulate the two-phase flow area (Fig. 2). The $y^+$ values of the mesh, at the center of the first cell, vary between 12 and 27 for a non cavitating computation.

According to the study of mesh dependence presented in [35], this grid size is adequate to simulate cavities in such Venturi type section.

## 4.3. Numerical parameters

For the non cavitating regime, computations are started from an uniform flow-field using a local time step. The numerical parameters used are:

- the CFL number, 10

- Jacobi iterations for the implicit stage, 15

- the two coefficients of the artificial dissipation, $k^{(2)} = 0$ and $k^{(4)} = 0.032$

- the farfield value of turbulent kinetic energy, $k_\infty = 0.0045$ m$^2$/s$^2$

- the farfield value of length, $l_\infty = 1.4\,10^{-6}$ m

For the unsteady cavitating regime, computations are performed with the dual time stepping method and are started from the non cavitating numerical solution. The numerical parameters are:

- the dimensionless time step, $\Delta t^* = \dfrac{\Delta t U_{inlet}}{L_{ref}} = 4.88\,10^{-3}$

- sub-iterations of the dual time stepping method, 100

- the CFL number, 0.2

- Jacobi iterations for the implicit stage, 15

- the two coefficients of the artificial dissipation, $k^{(2)} = 1$ and $k^{(4)} = 0.045$.

## 4.4. Global analysis

The unsteady calculations performed with the different derivations of the $k - \ell$ model are summarized in Table (I). The goal is to obtain a quasi-stable sheet cavity whose length varies between 70 and 85 mm and with a re-entrant jet. The time of simulation is between 1 and 3 seconds. For all calculations, the cavitation parameter in the inlet section is close to the experimental value and the length of the cavity is about 0.7 cm. Without surprise, the standard Smith $k - \ell$ model provides a steady solution. Both SST and realizable models with the usual value $c = 0.3$ also simulate a steady cavity. On the other hand, the reduction of the constant $c$ from 0.3 to 0.2 make possible to simulate a quasi stable sheet cavity. With the value $c = 0.1$, a cavity with vapour cloud shedding up to $x = 0.1$ m is obtained. As observed with the $k - \varepsilon$ and Spalart-Allmaras models, the Reboud correction improves the capability of the models to compute a realistic sheet [9]. As expected, the $k - \ell$ SAS model is able to correctly capture an unsteady quasi-stable sheet. All models including a turbulent viscosity reduction, except for the $k - \ell$ SST model with $c = 0.1$, show an attached cavity of 0.3 m long and a time-averaged length of the cavity of about 0.075 m, in good agreement with experimental visualizations.

## 4.5. Velocity and void ratio profiles

The local analysis involves void ratio and velocity profile comparisons inside the cavity. The experimental void ratio and velocity profiles are obtained for five stations by a double optical probe (Fig. 1). The velocity is evaluated as the most probable value and the void ratio is obtained from the signal of the double optical probe using a post-processing algorithm. The relative uncertainty on the void ratio measurement was estimated at roughly 15% [34]. All numerical values are obtained by a time-averaged treatment.

*4.5.1. Influence of the parameter $c$ on the SST and realizable models* The first comparisons concern the standard Smith model, the SST and realizable models with $c = 0.3$. Figure 3 shows the longitudinal velocity and void ratio profiles for the experiments and the three computations.

At the first two stations (not presented here), all models show a good agreement with the

experimental results. In particular, the void ratio is close to unity. At station 3, the experimental results show a re-entrant jet near the wall whereas none of the models simulate this phenomenon. All models predict an attached sheet cavity identical to the first two stations. Station 4 shows a difference between the standard $k - \ell$ model and the SST and realizable models. These last ones capture a small re-entrant jet with a velocity profile close to the experimental profile while the standard $k - \ell$ model computes a stable sheet. The last station indicates that both SST and realizable models compute a sheet that is too small compared to the experimental sheet.

From these comparisons, we note that the SST and realizable models with $c = 0.3$ initiate a small re-entrant jet. The standard Smith model is not able to predict unsteady behaviour.

To further reduce the eddy-viscosity, we decreased the $c$ value from 0.3 to 0.2 and 0.1, only in the two-phase flow region. Figure 4 shows the velocity and void ratio profiles for the experiment and four calculations: the SST model with $c = 0.3$, $c = 0.2$ and $c = 0.1$ and the realizable model with $c = 0.2$. At the first two stations (not presented here), the velocity and the void ratio profiles computed by all models are close to the experimental data. At station 3, the models with a $c$ value lower than 0.3 initiate a re-entrant jet. These models provide a velocity profile close to the experimental profile with a recirculation area thicker for the $k - \ell$ SST-$c = 0.1$ model than for the $k - \ell$ SST and realizable models with $c = 0.2$. The computed void ratio is well simulated with the SST-$c = 0.1$ model and overestimated by both SST and realizable models with $c = 0.2$. Velocity and void ratio profiles at station 4 indicate good agreement between the experiment and numerical computations. At station 5, the velocity profile computed with the SST-$c = 0.1$ model is close to the experimental data whereas recirculation is too weak for all other models. Therefore, only the $k - \ell$ SST model with $c = 0.1$ simulates a mixture area at this station. In the other cases, the sheet cavity length is too short.

On the whole, the use of the vorticity $\Omega$ or the stress tensor $S$ in the eddy-viscosity formulation does not change the numerical results computed. The velocity or the void ratio profiles obtained with both the SST and realizable models with the same $c$ value are very close.

The reduction of the viscosity limiter allows the development of a re-entrant jet and it seems that the $k - \ell$ SST model with $c = 0.1$ provides the best agreement with the experimental profiles. However, the dynamic behaviour of the sheet presents vapour cloud shedding (Fig. 10), which is not observed experimentally.

*4.5.2. Comparison of the Reboud correction and the SAS model* The velocity and the void ratio profiles obtained with the Reboud limiter and the SAS model are shown in Fig. 5. For comparison, we add the results provided by the SST model with $c = 0.2$.

As previously, the velocity and void ratio profiles at station 1 are identical for all models and close to the experimental results. At station 2 the velocity profile obtained with the SAS model shows a slight discrepancy with the experimental results due to an early re-entrant jet.

At station 3, both Reboud and SAS $k - \ell$ models predict a similar recirculation area. The void ratio profile computed by these models is close to the experimental data with overestimation at the wall. At station 4, both models provide identical solutions. The velocity curves match the experimental profile and the void ratios show the same trend as the experimental results though somewhat overestimated. The cavity computed by the SAS model is too short as we can see on the void ratio profile at station 5 contrary to the one computed by the $k - \ell$ Reboud model. However, the velocity profiles estimated by both models match the experimental results.

In conclusion, the $k - \ell$ SAS model and the $k - \ell$ model with the Reboud correction provide similar results close to the experimental data.

*4.6. Wall pressure evolution and RMS fluctuations*

The dimensionless wall pressure distribution $\frac{P - P_{vap}}{P_{vap}}$ is plotted in Fig. 6 versus the distance $x - x_{inlet}$. The first five data are located inside the cavity (where the void ratio and velocity profiles are measured).

All models provide a pressure distribution similar to the experimental measurements upstream of the re-compression. The re-compression computed by all models is too strong. Moreover, the standard model, the $k - \ell$ SST model with $c = 0.1$ and the SAS model compute a re-compression that is

slightly too far downstream compared to the experimental observations.

The Root Mean Square (RMS) wall pressure fluctuations are plotted in Fig. 7 versus the distance $x - x_{inlet}$. The pressure fluctuation is divided by the time-averaged pressure $Pav$. For all computations, the statistical treatment is performed over a simulation time of 1 to 3 s. Experimental data indicate an augmentation of pressure fluctuations at the end of the sheet cavity, with a peak located at the fifth station.

The standard model and both the SST and realizable models with $c = 0.3$ yield a pressure fluctuation profile close to the experimental profile even if the peak is slightly overestimated and the pressure fluctuation range is narrower. The pressure fluctuation computed by the $k - \ell$ Reboud model presents a different behaviour with two peaks more than three times higher than the experimental peak. The $k - \ell$ SST model with $c = 0.2$ and $c = 0.1$ also provides an overestimated pressure peak. The pressure fluctuations range for the $k - \ell$ SST model with $c = 0.1$ is too large. Finally, the profile simulated by the $k - \ell$ SAS model is in good agreement with the experimental data even if the peaks are overestimated.

*4.7. Turbulent eddy-viscosity profiles*

Figure 8 compares time-averaged profiles of the viscosity ratio $\mu_t/\mu$, at the five stations, obtained with the $k - \ell$ SST model with $c = 0.2$ and $c = 0.1$, the $k - \ell$ model with the Reboud correction and the $k - \ell$ SAS model.

First, the $k - \ell$ model with the Reboud correction induces a large reduction of the ratio $\mu_t/\mu$ in the sheet at all stations except at station 5. This model always shows the same $\mu_t/\mu$ shape with a peak of the ratio at the boarder between pure liquid flow and the cavity followed by a quick decrease. The peak never exceeds the value of ten. Nevertheless, this drastic reduction of the $\mu_t/\mu$ ratio compared to the other models seems to be unnecessary to correctly simulate a re-entrant jet.

The ratio computed by the $k - \ell$ SST-$c = 0.1$ model is bounded by the $k - \ell$ Reboud and $k - \ell$ SAS models. However, the $k - \ell$ SST-$c = 0.1$ sheet (Fig 10) shows vapour cloud shedding which is not

observed with the other models. Consequently, an eddy-viscosity reduction leads to different sheet cavity behaviours according to how this reduction is set in the model.

### 4.8. Density gradient and Q-criterion

We now propose a qualitative description of the dynamics of sheet cavities with plotting of the contours of the density gradient modulus (Schlieren-like visualizations) and the iso-lines of the Q-criterion. Four calculations at three different times are studied: the $k - \ell$ SST model with $c = 0.2$ (Fig 9) and with $c = 0.1$ (Fig 10), the $k - \ell$ SAS model (Fig 11) and the $k - \ell$ Reboud model (Fig 12).

The Schlieren-like visualizations give some information about the sheet. First, all models simulate a stable attached cavity signaled by a strong density gradient from the abscissa $x = 0$ m up to approximately $x = 0.035$ m for the SST model with $c = 0.2$ and $x = 0.025$ m for the other calculations. This cavity is followed by a time-fluctuating two-phase area, which differs according to the model. The $k - \ell$ SST model with $c = 0.1$ (Fig 10) provides cavitation cloud shedding not observed either in the experiment or in other computations. The end of the $k - \ell$ Reboud cavity (Fig 12) fluctuates slightly between $x = 0.75$ m and $x = 0.85$ m whereas the $k - \ell$ SST model with $c = 0.2$ (Fig 9) and the $k - \ell$ SAS model (Fig 11) do not show such fluctuations. The quasi-stable sheet computed by the $k - \ell$ SST $c = 0.2$ and $k - \ell$ Reboud models provides strong density gradients inside the cavity and a shear layer is clearly exhibited. On the other hand, the SAS model simulates a more homogeneous cavity.

Positive values of the Q-criterion, defined as the second invariant of the velocity gradient tensor $\frac{\partial u_i}{\partial x_j}$ [36],

$$Q = \frac{1}{2}\left[\left(\frac{\partial u_i}{\partial x_i}\right)^2 - \frac{\partial u_i}{\partial x_j}\frac{\partial u_j}{\partial x_i}\right] \tag{23}$$

are used to identify vortices and local rotational areas. A dimensionless quantity is built using the inlet velocity and the reference length. Iso-line levels vary between 0.004 and 0.01.

All models simulate a shear layer at the boundary between the stable and quasi-stable parts of the sheet. Vortex shedding occurs along the boundary between the external flow and the recirculating flow. The extension of the shear layer differs according to the model.

## 5. CONCLUSION

An aperiodic quasi stable sheet cavity has been studied in a 2D Venturi configuration by numerical one-fluid RANS simulations. Numerical results have been compared with experimental data concerning the void ratio, streamwise velocity, wall pressure and wall pressure fluctuations. Calculations have been carried out with the Smith $k - \ell$ turbulence model with different eddy-viscosity limitation strategies: the SST limiter developed by Menter, a realizability constraints correction as developed by Durbin, the Reboud correction specially built for cavitating flows and a Scale-Adaptive Simulation model based on Menter's work. Moreover, tests on the values of the SST or realizable limiter have been carried out in order to further reduce the eddy-viscosity.

Results show that the use of an eddy-viscosity limiter lets the model correctly simulate unsteady behaviours of the sheet, however large discrepancies occur between models. First, reduction of the parameter $c$ in both the SST and realizable models has shown that it is possible to tune this constant to obtain an adequate solution. Indeed, a value of $c = 0.1$ leads to a cavity with vapour cloud shedding whereas a value of $c = 0.2$ leads to an underestimation of re-entrant jet development. Therefore, an intermediate value should give results in good agreement with experimental observations. However, it is likely that this value depends on the geometry.

On the other hand, the Reboud correction and the SAS model provide local profiles in good agreement with the experimental data. The RMS pressure fluctuations reveal some differences between models. With the Reboud correction, the peak of wall fluctuations is largely overestimated. The topology of the cavity illustrated by density gradient visualizations also shows some differences. The SAS computation leads to a more homogeneous cavity in comparison with the Reboud solution. Furthermore, the drastic reduction of the eddy-viscosity caused by the Reboud correction compared to other models seems to be unnecessary to simulate an unsteady sheet cavity.

Note that the $k - \ell$ SAS model provides good results since it does not use an ad hoc correction to force the model to reproduce the experimental flow. The SAS formulation introduces additional information from the mean velocity profile to reduce the eddy-viscosity through an added destruction term in the $\ell$ transport equation. Consequently, this model has a more robust physical basis. Its good behaviour in cavitating flows needs to be confirmed by performing three-dimensional computations and other geometries.

*Prepared using fldauth.cls*

## REFERENCES

1. Reboud JL, Stutz B, Coutier O. Two-phase flow structure of cavitation: experiment and modelling of unsteady effects. *$3^{rd}$ International Symposium on Cavitation CAV1998, Grenoble, France*, 1998.

2. Coutier-Delgosha O, Fortes-Patella R, Reboud J. Simulation of unsteady cavitation with a two-equation turbulence model including compressibility effects. *Journal of Turbulence* 2002; **3**(58).

3. Chen Y, Lu C, Wu L. Modelling and computation of unsteady turbulent cavitation flows. *Journal of Hydrodynamics* 2006; **18**(5):559–566.

4. Wilcox D. Turbulence modeling for CFD. DCW Industries Inc. 1998.

5. Vaidyanathan R, Senocak I, Wu J, Shyy W. Sensitivity evaluation of a transport-based turbulent cavitation model. *Journal of Fluids Engineering* 2003; **125**(5):447–458.

6. Wu J, Wang G, Shyy W. Time-dependent turbulent cavitating flow computations with interfacial transport and filter-based models. *Int. Journal for Numerical Methods in Fluids* 2005; **49**(7):739–761.

7. Goncalves E, Patella RF. Numerical simulation of cavitating flows with homogeneous models. *Computers & Fluids* 2009; **38**(9):1682–1696.

8. Goncalves E, Patella RF. Numerical study of cavitating flows with thermodynamic effect. *Computers & Fluids* 2010; **39**(1):99–113.

9. Goncalves E. Numerical study of unsteady turbulent cavitating flows. *European Journal of Mechanics B/Fluids* 2011; **30**(1):26–40.

10. Smith B. A near wall model for the $k − l$ two equation turbulence model. *AIAA 94–2386, $25^{sh}$ Fluid Dynamics Conference – Colorado Springs, Colorado*, 1994.

11. Menter F. Zonal two equation $k − \omega$ turbulence models for aerodynamic flows. *AIAA 93–2906, 24th Fluid Dynamics Conference – Orlando, Florida*, 1993.

12. Menter F. Two-equation eddy-viscosity turbulence models for engineering applications. *AIAA Journal* 1994; **32**(8):1598–1605.

13. Durbin P. Limiters and wall treatments in applied turbulence modeling. *Fluid Dyn. research* 2009; **41**(1):012 203.

14. Menter F, Egorov Y. A scale-adaptive simulation model using two-equation models. *AIAA 2005–1095, 43rd Aerospace Science Meeting and Exhibit, Reno, Nevada*, 2006.

15. Menter F. The scale-adaptive simulation mathod for unsteady turbulent flow predictions. part 1: Theory and model description. *Flow, Turbulence and Combustion* 2010; **85**(1):113–138.

16. Menter F. Eddy viscosity transport equations and their relation to the $k − \epsilon$ model. *Journal of Fluids Engineering* 1997; **119**:876–884.

17. Menter F, Egorov Y. Re-visiting the turbulent scale equation. *Proceeding IUTAM Symposium; One hundred years of boundary layer research – Gottingen*, 2004.

18. Menter F. The scale-adaptive simulation mathod for unsteady turbulent flow predictions. part 2: Application to complex flows. *Flow, Turbulence and Combustion* 2010; **85**(1):139–165.

19. Davidson L. Evaluation of the sst-sas model: channel flow, asymmetric diffuser and axi-symmetric hill. *Proceedings of ECCOMAS CFD 2006, Egmond aan Zee, The Netherlands*, 2006.

20. Guillard H, Viozat C. On the behaviour of upwind schemes in the low Mach number limit. *Computers & Fluids* 1999; **28**(1):63–86.

21. Turkel E. Preconditioned methods for solving the incompressible and low speed compressible equations. *Journal of Computational Physics* 1987; **172**(2):277–298.

22. Delannoy Y, Kueny J. Two phase flow approach in unsteady cavitation modelling. *Cavitation and Multiphase Flow Forum, ASME-FED, vol. 98, pp.153-158*, 1990.

23. Smith B. The $k - kl$ turbulence model and wall layer model for compressible flows. *AIAA 90–1483*, $21^{st}$ *Fluid and Plasma Dynamics Conference – Seattle, Washington*, 1990.

24. Huang P, Coleman G, Bradshaw P. Compressible turbulent channel flows: Dns results and modelling. *Journal of Fluid Mechanics* 1995; **305**:185–218.

25. Sarkar S. The stabilizing effect of compressibility in turbulent shear flow. *Journal of Fluid Mechanics* 1995; **282**:163–186.

26. Lechner R, Sesterhenn J, Friedrich R. Turbulent supersonic channel flow. *Journal of Turbulence* 2001; **2**(1).

27. Viegas J, Rubesin M. Wall–function boundary conditions in the solution of the Navier–Stokes equations for complex compressible flows. *AIAA 83–1694*, $16^{th}$ *Fluid and Plasma Dynamics Conference – Danver, Massachussetts*, 1983.

28. Aeschlimann V, Barre S. PIV-LIF determination of mean velocity field and Reynolds stress tensor in a cavitating mixing layer. $7^{th}$ *International Symposium on Cavitation CAV2009, Ann Arbor, USA*, 2009.

29. Jameson A, Schmidt W, Turkel E. Numerical solution of the Euler equations by finite volume methods using Runge-Kutta time stepping schemes. *AIAA Paper 81–1259*, 1981.

30. Roe P. Approximate Riemann solvers, parameters vectors, and difference schemes. *Journal of Computational Physics* 1981; **43**:357–372.

31. Tatsumi S, Martinelli L, Jameson A. Flux-limited schemes for the compressible Navier-Stokes equations. *AIAA Journal* 1995; **33**(2):252–261.

32. Luo H, Baum J, Lohner R. A fast, matrix-free implicit method for compressible flows on unstructured grids. *Journal of Computational Physics* 1998; **146**(2):664–690.

33. Merci B, Steelant J, Vierendeels J, Riemslagh K, Dick E. Computational treatment of source terms in two-equation turbulence models. *AIAA Journal* 2000; **38**(11):2085–2093.

34. Barre S, Rolland J, Boitel G, Goncalves E, Patella RF. Experiments and modelling of cavitating flows in Venturi: attached sheet cavitation. *European Journal of Mechanics B/Fluids* 2009; **28**:444–464.

35. Coutier-Delgosha O, Patella RF, Reboud J, Hakimi N, Hirsch C. Numerical simulation of cavitating flow in 2D and 3D inducer geometries. *Int. Journal for Numerical Methods in Fluids* 2005; **48**:135–167.

36. Hunt J, Wray C, Moin P. Eddies, streams, and convergence zones in turbulent flows. *Technical Report*, Center for Turbulence Research, CTR-S88 1988.

*Prepared using fldauth.cls*

Table I. Unsteady computations, 4° Venturi.

| case | turbulence model | $\sigma_{inlet}$ | comments | sheet length (m) |
|---|---|---|---|---|
| 1 | KL | 0.59 | steady state | 0.075 |
| 2 | KL + Reboud | 0.56 | aperiodic quasi stable sheet | 0.080 |
| 3 | KL + SST c = 0.3 | 0.59 | steady state | 0.070 |
| 4 | KL + SST c = 0.2 | 0.59 | aperiodic quasi stable sheet | 0.070 |
| 5 | KL + SST c = 0.1 | 0.58 | aperiodic quasi stable sheet | 0.100 |
| 6 | KL + Durbin c = 0.3 | 0.59 | steady state | 0.070 |
| 7 | KL + Durbin c = 0.2 | 0.59 | aperiodic quasi stable sheet | 0.070 |
| 8 | KL + SAS | 0.58 | aperiodic quasi stable sheet | 0.070 |
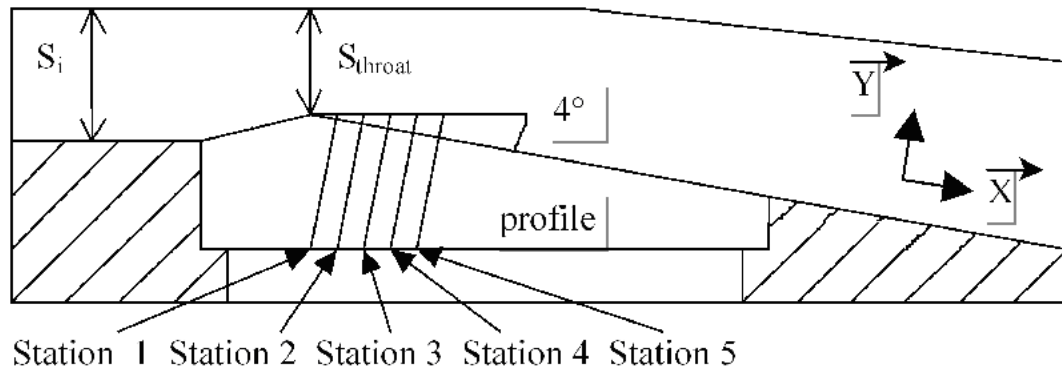
Figure 1. Schematic view of the $4°$ Venturi profile.
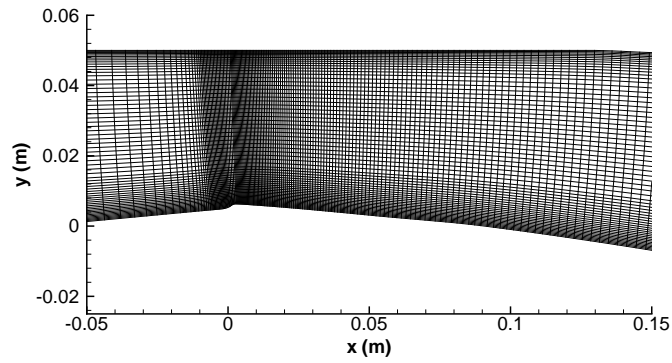
Figure 2. Enlargement of the mesh near the Venturi throat.
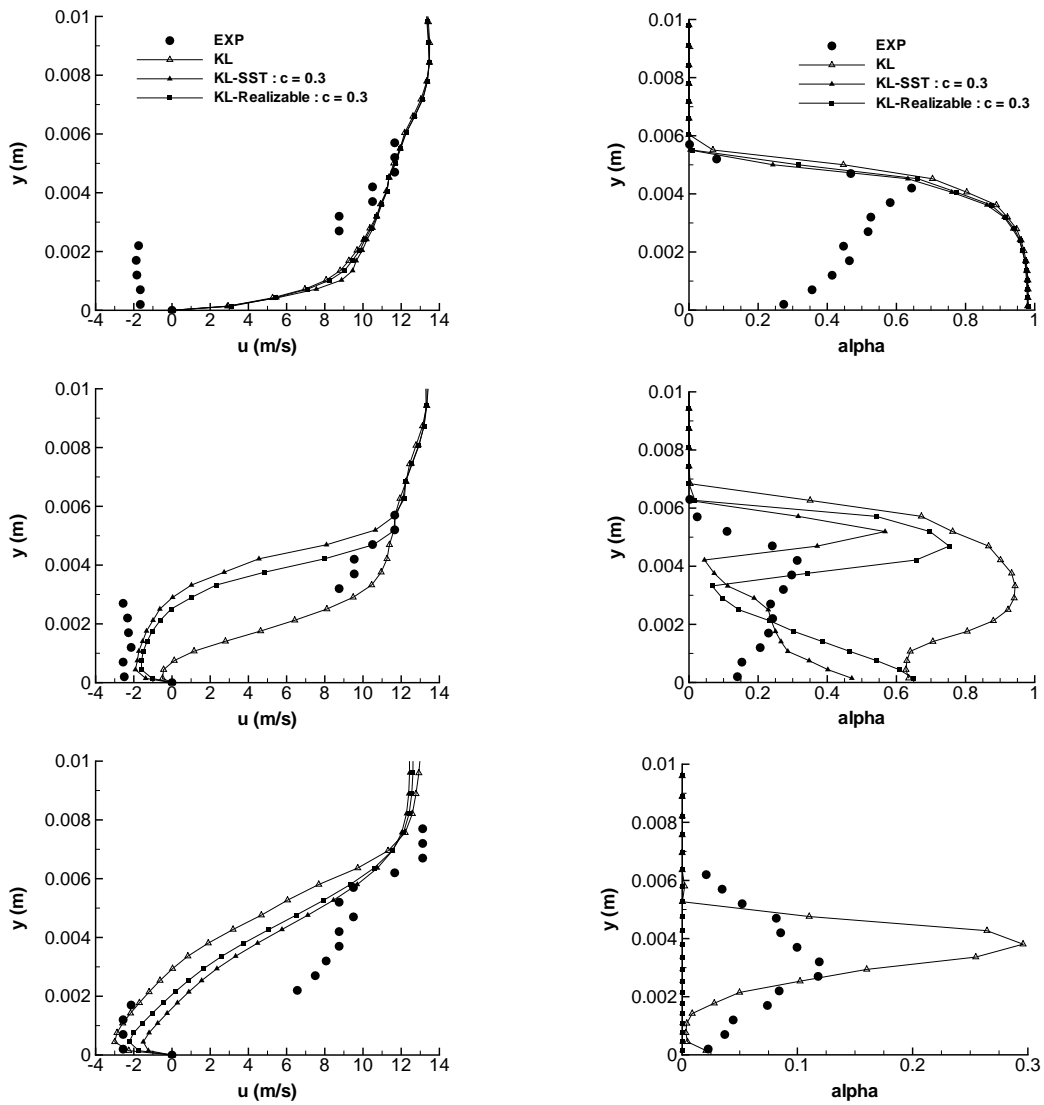
Figure 3. Velocity (left) and void ratio (right) profiles from station 3 to 5.
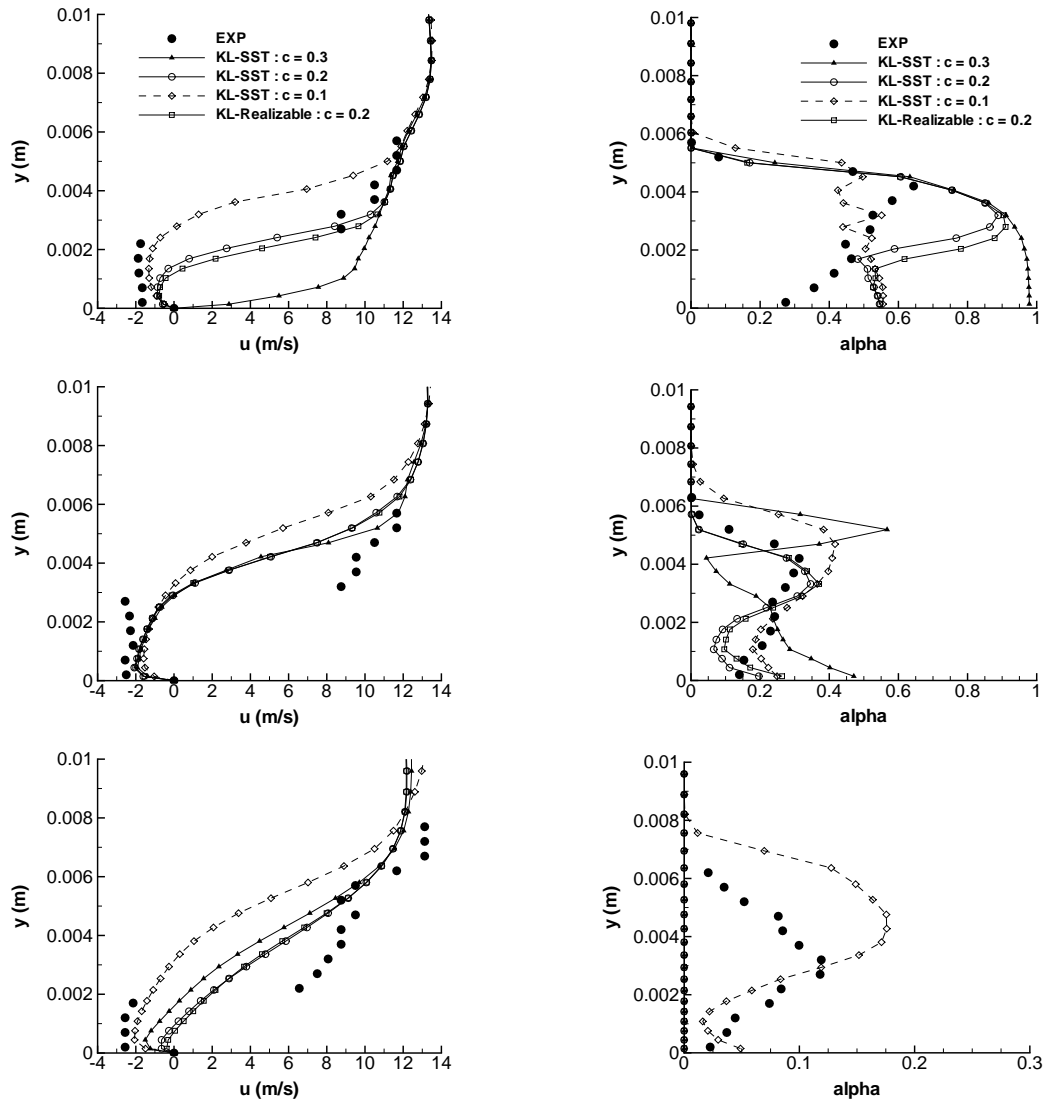
Figure 4. Velocity (left) and void ratio (right) profiles from station 3 to 5.
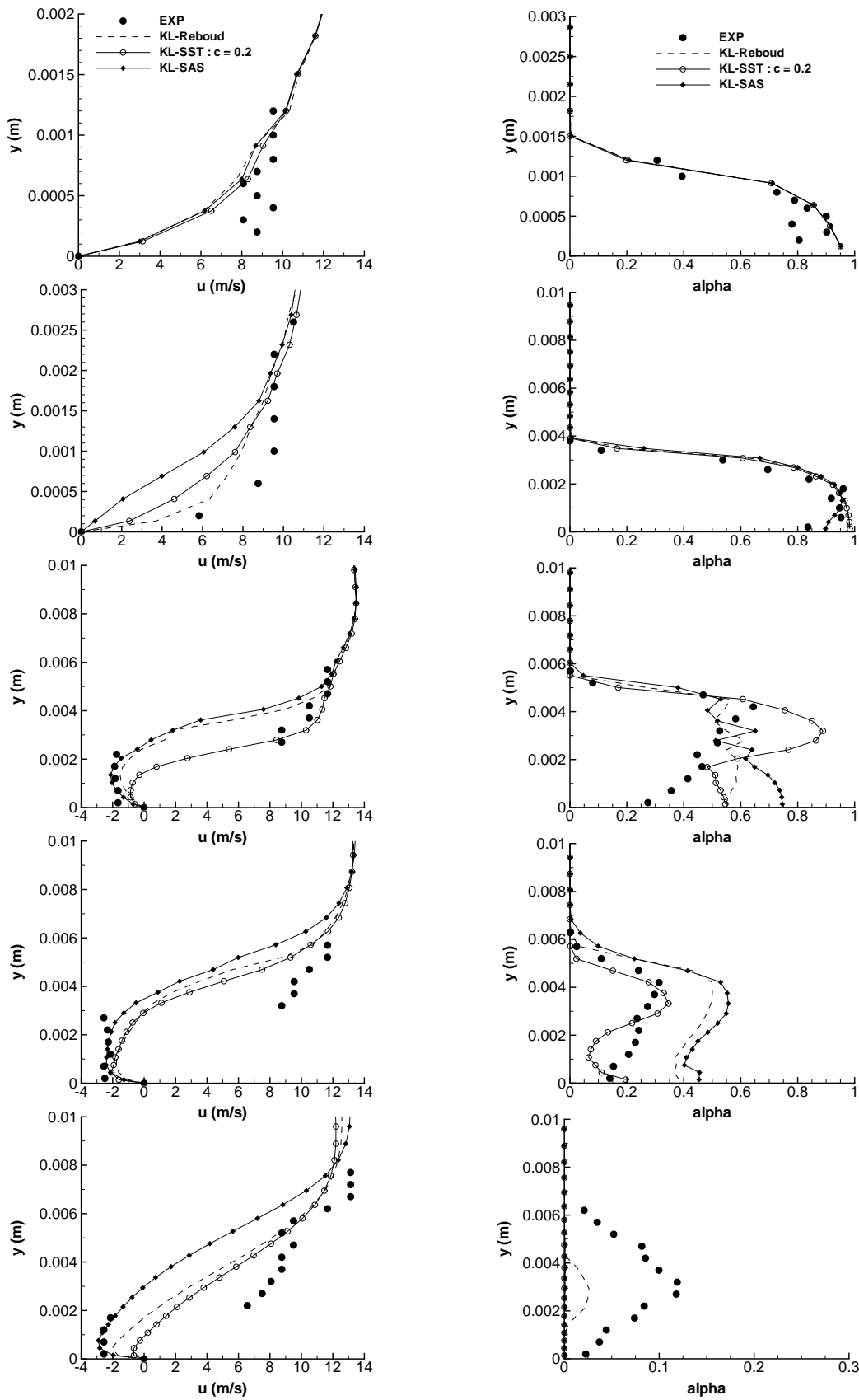
Figure 5. Velocity (left) and void ratio (right) profiles from station 1 to 5.
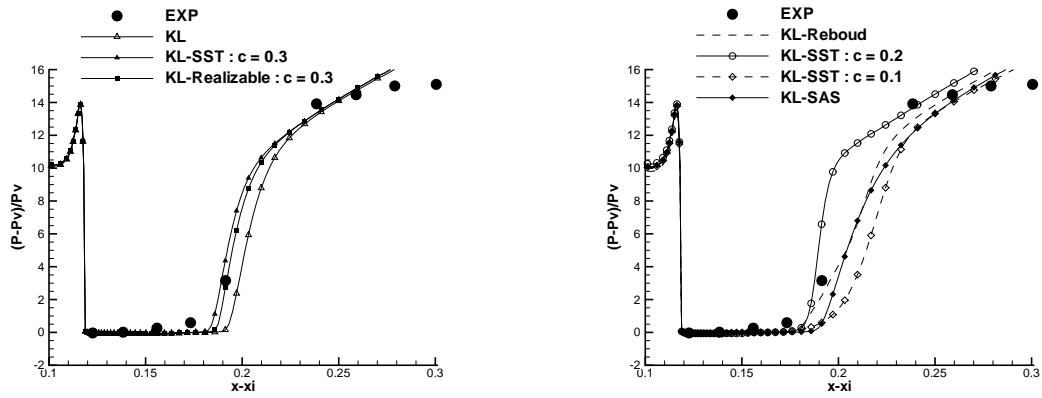
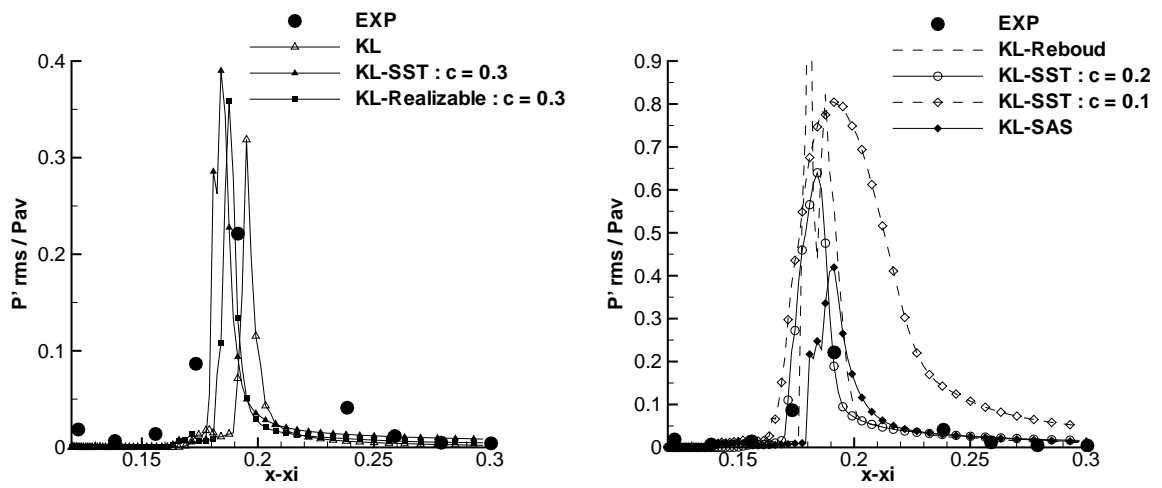Figure 6. Dimensionless wall pressure evolution.
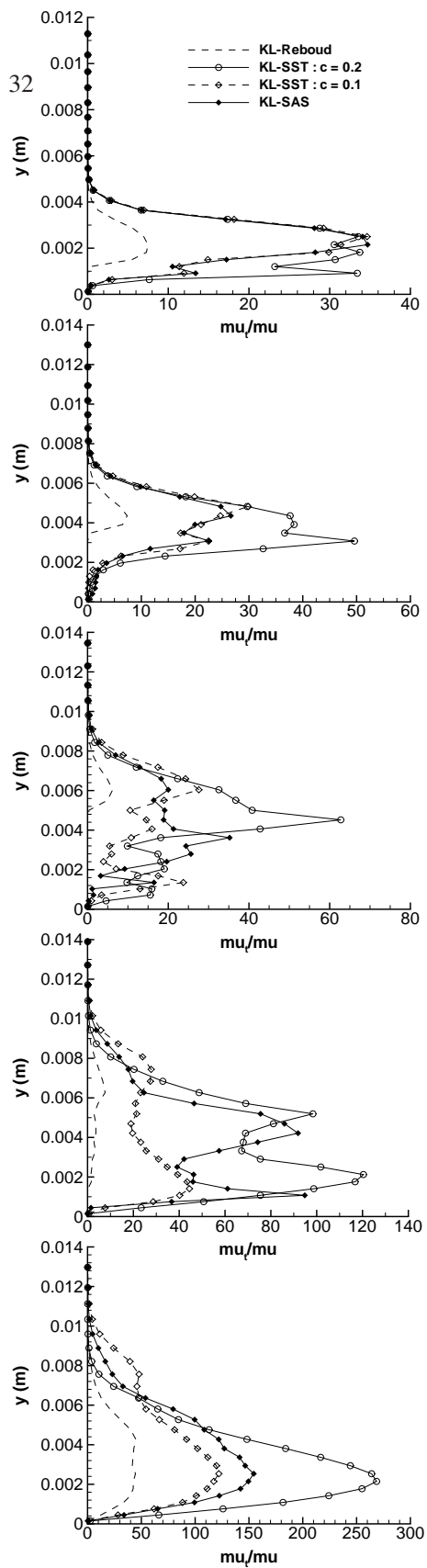
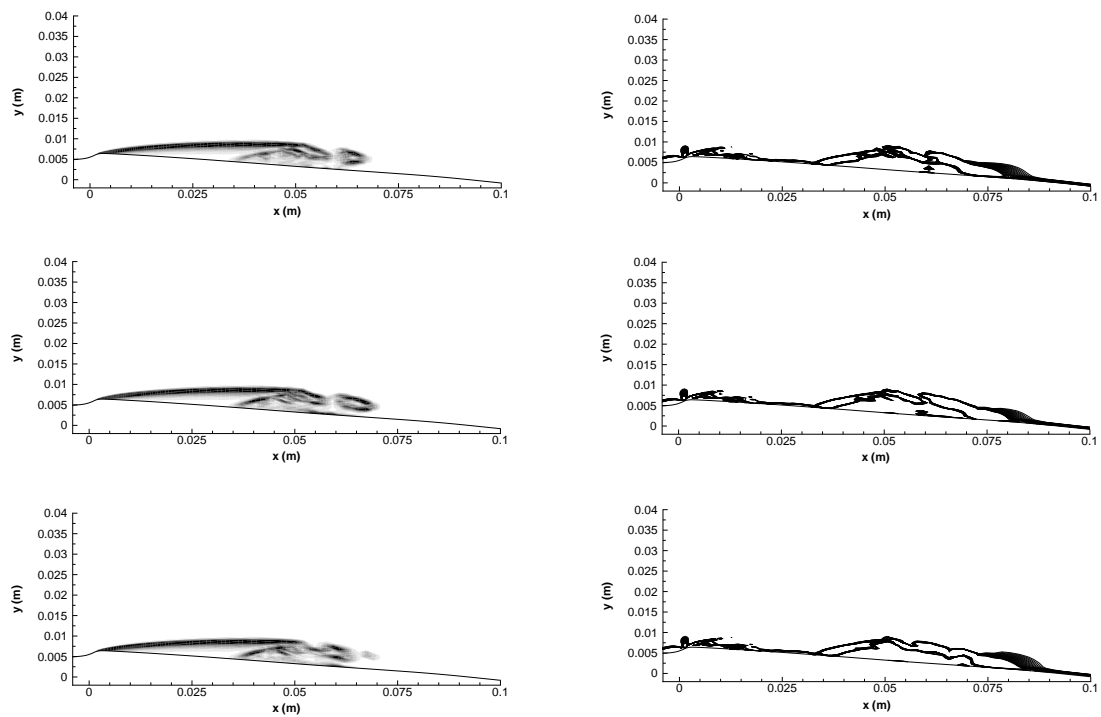Figure 7. RMS wall pressure fluctuations.

Figure 8. Time averaged $\mu_t/\mu$ profiles from station 1 to 5.

Figure 9. Contours of the density gradient (left) and iso-lines of the dimensionless Q-criterion (right), at three instants, KL-SST c = 0.2 model.
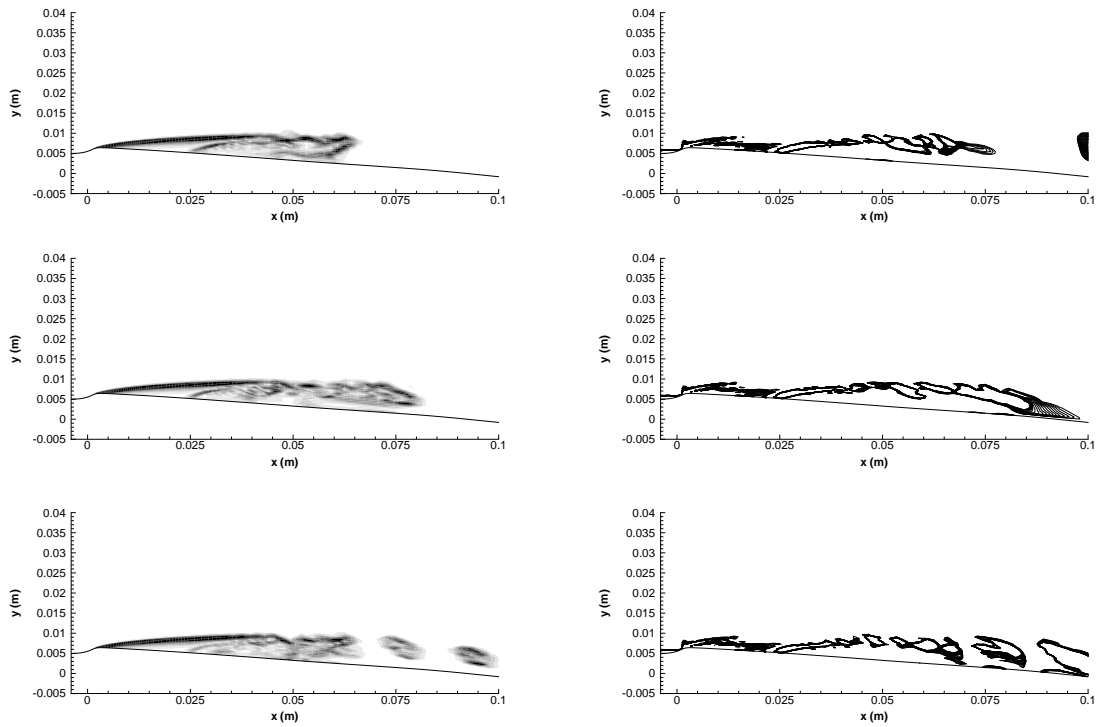
Figure 10. Contours of the density gradient (left) and iso-lines of the dimensionless Q-criterion (right), at three instants, KL-SST c = 0.1 model.
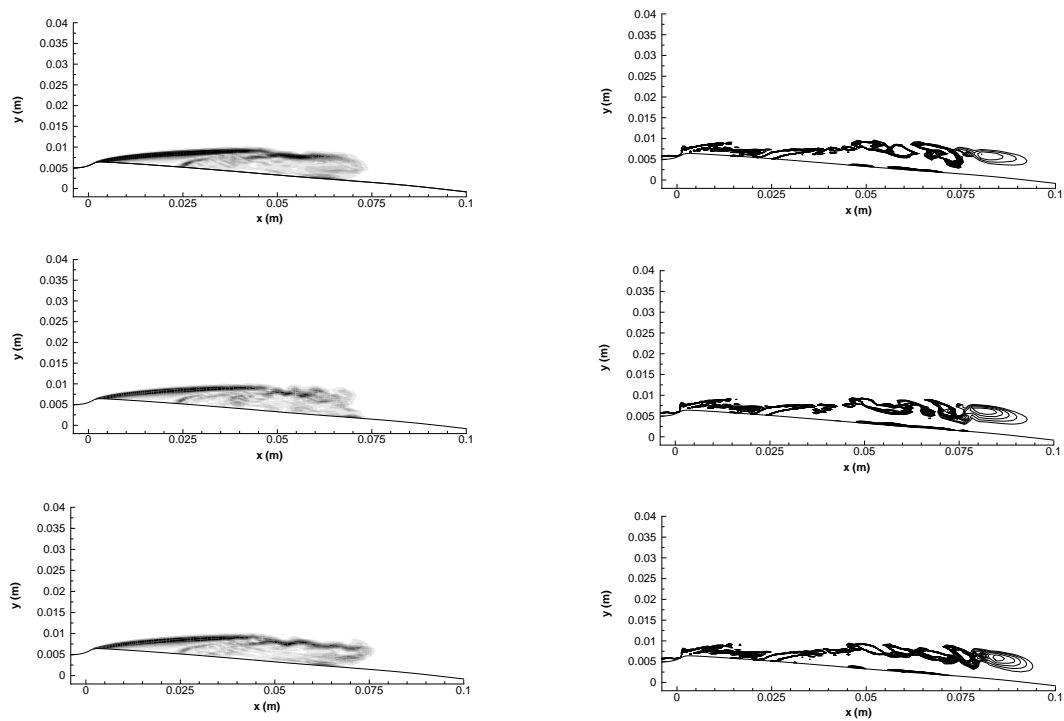
Figure 11. Contours of the density gradient (left) and iso-lines of the dimensionless Q-criterion (right), at three instants, KL-SAS model.
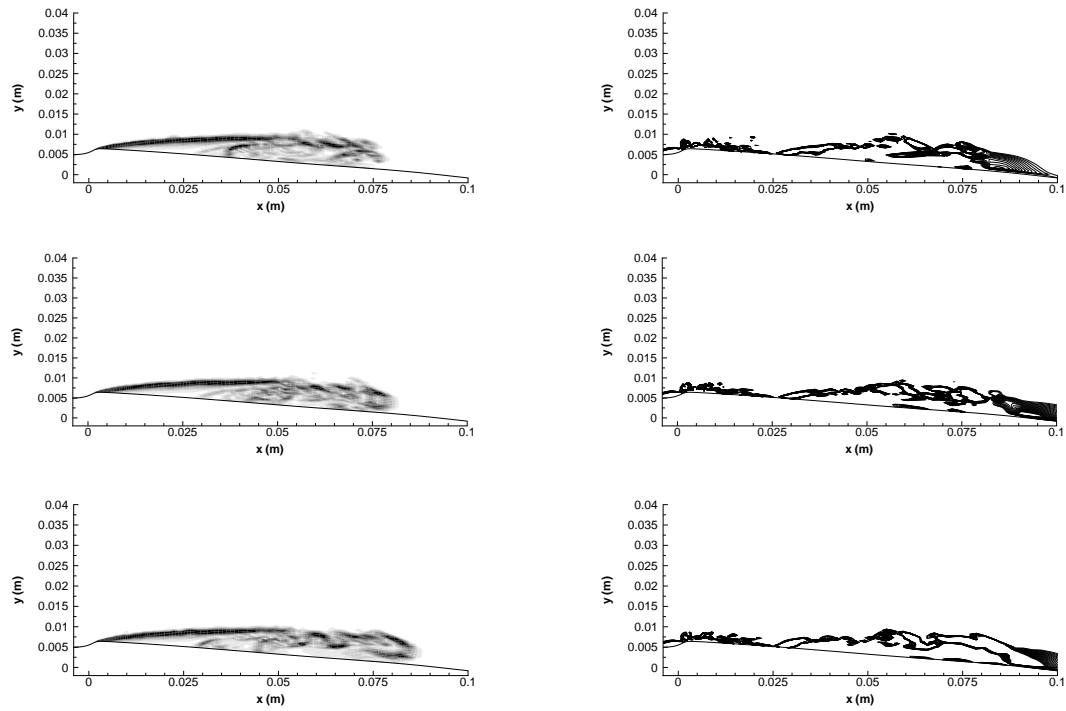
Figure 12. Contours of the density gradient (left) and iso-lines of the dimensionless Q-criterion (right), at three instants, KL-Reboud model.

*Prepared using fldauth.cls*